

## ARTICLE OPEN



# Ambient effect on the Curie temperatures and magnetic domains in metallic two-dimensional magnets

Zhiyin Tu<sup>1,7</sup>, Ti Xie<sup>1,7</sup>, Yeonghun Lee<sup>2</sup>, Jinling Zhou<sup>3,4</sup>, Alemayehu S. Admasu<sup>5</sup>, Yu Gong<sup>6</sup>, Nagarajan Valanoor<sup>4</sup>, John Cumings<sup>3</sup>, Sang-Wook Cheong<sup>5</sup>, Ichiro Takeuchi<sup>3</sup>, Kyeongjae Cho<sup>2</sup> and Cheng Gong<sup>1</sup>✉

The emergent magnetic two-dimensional (2D) materials provide ideal solid-state platforms for a broad range of applications including miniaturized spintronics, nonreciprocal optics, and magnetoelectric sensors. Owing to the general environmental sensitivity of 2D magnets, the understanding of ambient effects on 2D magnetism is critical. Apparently, the nature of itinerant ferromagnetism potentially makes metallic 2D magnets insensitive to environmental disturbance. Nevertheless, our systematic study showed that the Curie temperature of metallic 2D  $\text{Fe}_3\text{GeTe}_2$  decreases dramatically in the air but thick  $\text{Fe}_3\text{GeTe}_2$  exhibits self-protection. Remarkably, we found the air exposure effectively promotes the formation of multiple magnetic domains in 2D  $\text{Fe}_3\text{GeTe}_2$ , but not in bulk  $\text{Fe}_3\text{GeTe}_2$ . Our first-principles calculations support the scenario that substrate-induced roughness and tellurium vacancies boost the interaction of 2D  $\text{Fe}_3\text{GeTe}_2$  with the air. Our elucidation of the thickness-dependent air-catalyzed evolution of Curie temperatures and magnetic domains in 2D magnets provides critical insights for chemically decorating and manipulating 2D magnets.

npj 2D Materials and Applications (2021)5:62; <https://doi.org/10.1038/s41699-021-00242-z>

## INTRODUCTION

The discovery of magnetic 2D van der Waals (vdW) materials<sup>1–5</sup> ushered the long-range magnetic order into atomic-thin crystals, presenting unique solid-state platforms where magnetic order and structural order coexist and couple mutually in the ultrathin regime. Therefore, any relevant factors that impact the atomic structures of 2D flatlands can affect the 2D magnetism. One remarkable feature of 2D materials is the extreme surface-to-bulk ratio, which means 2D materials are altogether open to the environments and thus easily accessible by gas molecules or chemicals<sup>6,7</sup>. The interaction between 2D materials and the ambient (especially  $\text{O}_2$  and  $\text{H}_2\text{O}$  molecules) represents one possible scenario that explains the instability of many 2D materials such as black phosphorene<sup>8,9</sup> and  $\text{CrI}_3$ <sup>10</sup> in the air.

Elucidating the evolution of 2D magnets in the air would deliver practical guidance on how to protect 2D magnets and how to rationally engineer 2D magnetic properties. It is intuitive to speculate that metallic 2D magnets may be robust against environmental disturbance or local defects, as the itinerant electrons—that is, the free carriers responsible for the ferromagnetic mediation—can circumvent local atomic-scale defects<sup>11</sup>. However, an already known phenomenon of stoichiometry-dependent Curie temperature of  $\text{Fe}_{3-x}\text{GeTe}_2$ <sup>12–14</sup> suggests the sensitive role of defects in metallic 2D magnets. Furthermore, the large variance in the reported Curie temperatures of 2D  $\text{Fe}_3\text{GeTe}_2$  of nominally the same thickness<sup>15–17</sup> indicates how sensitively the properties of 2D  $\text{Fe}_3\text{GeTe}_2$  depend on the specific sample processing details.

Here, through the systematic reflectance magnetic circular dichroism (RMCD) studies of  $\text{Fe}_3\text{GeTe}_2$  of different thicknesses under controlled degrees of exposure to the air, we found thinner

$\text{Fe}_3\text{GeTe}_2$  (e.g., three or four layers) degrades dramatically but thicker  $\text{Fe}_3\text{GeTe}_2$  (e.g., eight layers or bulk) only exhibits a slight property change in the initial exposure and tends to stabilize afterward, which suggests the thick  $\text{Fe}_3\text{GeTe}_2$  becomes self-protected after the initial reactions with the air. More remarkably, in zero-field cooling experiments, the ambient-treated thick  $\text{Fe}_3\text{GeTe}_2$  exhibits high magnetization which indicates a single magnetic domain or merely a handful of magnetic domains, but the treated thin  $\text{Fe}_3\text{GeTe}_2$  exhibits low magnetization which indicates the formation of multiple magnetic domains.

## RESULTS

### Thickness characterization of few-layer $\text{Fe}_3\text{GeTe}_2$

In this work, we conducted all experiments based on a prototypical metallic vdW ferromagnet  $\text{Fe}_3\text{GeTe}_2$ <sup>15–20</sup>. We synthesized bulk  $\text{Fe}_3\text{GeTe}_2$  single crystals by chemical vapor transport method, and mechanically exfoliated few layers, and deposited them on 260-nm-thick- $\text{SiO}_2/\text{Si}$  chips. The bulk Curie temperature ( $T_C$ ) is at 190 K, agreeing well with Deng et al.'s prior work<sup>17</sup>. This suggests the presence of a small amount of Fe deficiency in the  $\text{Fe}_{3-x}\text{GeTe}_2$  crystal<sup>12</sup>. Layer numbers of 2D  $\text{Fe}_3\text{GeTe}_2$  samples were identified by examining the optical contrast and the Curie temperature (see Fig. 1). Figure 1a shows a linear dependence of optical contrast on layer numbers in the ultrathin region. The assignment of three and four layers (3 L and 4 L) to the two samples (optical images shown in the inset of Fig. 1a) is further confirmed by their  $T_C$  values of about 120 K and 145 K, similar to the previously reported  $T_C$  values of the 3 L and 4 L  $\text{Fe}_3\text{GeTe}_2$  of similar crystal stoichiometry with ours<sup>17</sup>. The thickness of the 8 L  $\text{Fe}_3\text{GeTe}_2$  is identified by the combination of atomic force

<sup>1</sup>Department of Electrical and Computer Engineering and Quantum Technology Center, University of Maryland, College Park, MD, USA. <sup>2</sup>Department of Materials Science and Engineering, The University of Texas at Dallas, Richardson, TX, USA. <sup>3</sup>Department of Materials Science and Engineering, University of Maryland, College Park, MD, USA. <sup>4</sup>School of Materials Science and Engineering, University of New South Wales, Sydney, Australia. <sup>5</sup>Rutgers Center for Emergent Materials and Department of Physics and Astronomy, Rutgers, The State University of New Jersey, Piscataway, NJ, USA. <sup>6</sup>Department of Physics and Astronomy, College of Charleston, Charleston, SC, USA. <sup>7</sup>These authors contributed equally: Zhiyin Tu, Ti Xie. ✉email: [gongc@umd.edu](mailto:gongc@umd.edu)

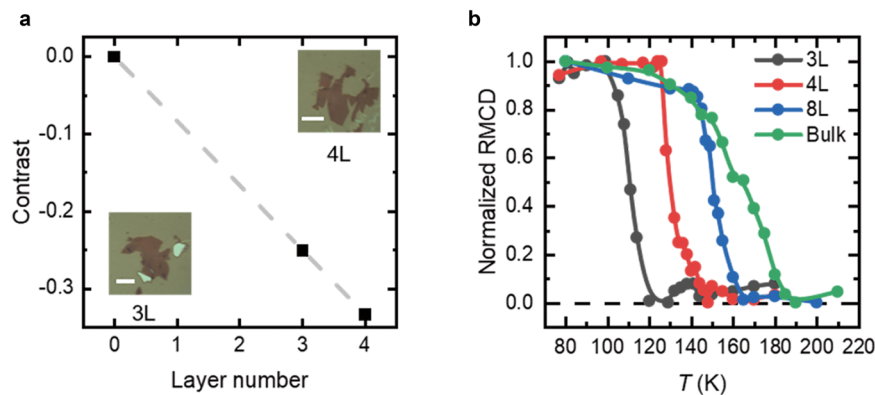


**Fig. 1 Optical images, optical contrasts, and the normalized RMCD of few-layer  $\text{Fe}_3\text{GeTe}_2$ .** **a** Gray channel optical contrasts and optical images of the 3 L and 4 L  $\text{Fe}_3\text{GeTe}_2$ . The optical contrasts of the 3 L and 4 L  $\text{Fe}_3\text{GeTe}_2$  follow the linear dependence on layer numbers. The gray dashed line serves as an eye guide. Scale bars in the insets, 5  $\mu\text{m}$ . **b** Normalized RMCD of  $\text{Fe}_3\text{GeTe}_2$  of different thicknesses. The  $T_C$  values of the 3 L and 4 L  $\text{Fe}_3\text{GeTe}_2$  are at about 120 K and 145 K, similar to the reported values in the previous literature<sup>17</sup>. The error bars are within the symbol size.

microscopy (AFM) and optical contrast analysis (see Supplementary Fig. 1 in the supplementary information).

### Ambient effect on the Curie temperatures of few-layer $\text{Fe}_3\text{GeTe}_2$

The  $\text{Fe}_3\text{GeTe}_2$  samples of different thicknesses were heated in the air at 50 °C for the study of the ambient effects. The term “treatment” hereafter denotes the heating at 50 °C in the air unless defined elsewhere. Given 50 °C does not suffice to trigger any phase change in  $\text{Fe}_3\text{GeTe}_2$  either between different crystal structures or between solid and liquid states, the difference between 50 °C and room temperature treatments can be simply reflected by the Arrhenius equation  $\kappa = A \exp(-E_a/k_B T)$  where  $\kappa$  is the reaction rate,  $A$  is the pre-exponential factor that describes the collision frequency of the “air molecules” with  $\text{Fe}_3\text{GeTe}_2$ ,  $k_B$  is the Boltzmann constant,  $T$  is the temperature, and  $E_a$  is the reaction energy barrier. Therefore, the heating duration at 50 °C can be translated to a longer duration of exposure to the air at room temperature, without extra complexity.

The  $\text{Fe}_3\text{GeTe}_2$  samples of different thicknesses behave distinctly upon the treatments. Figure 2a shows the  $T_C$  value of bulk  $\text{Fe}_3\text{GeTe}_2$  remains constant at 190 K after 30-min heating in the air. The  $T_C$  value of the 8 L  $\text{Fe}_3\text{GeTe}_2$  drops by about 10 K (from 165 K to 155 K) in the first 10-min treatment and continues to stay constant during additional 10-min and 20-min treatments (see Fig. 2b). This suggests the interior  $\text{Fe}_3\text{GeTe}_2$  is protected upon the initial reaction between the surface of the 8 L  $\text{Fe}_3\text{GeTe}_2$  and the ambient. In stark contrast, the  $T_C$  value of a 4 L  $\text{Fe}_3\text{GeTe}_2$  progressively decreases with the increased duration of treatments (untreated: 145 K; 10-min treatment: 132 K; 20-min treatment: 118 K; 30-min treatment: 90 K). More dramatically, the  $T_C$  value of a 3 L  $\text{Fe}_3\text{GeTe}_2$  quickly drops from 120 K to 100 K after only 5-min treatment. It is clear that 2D  $\text{Fe}_3\text{GeTe}_2$  degrades more dramatically than thicker or bulk  $\text{Fe}_3\text{GeTe}_2$ . The  $T_C$  drop of the 4 L  $\text{Fe}_3\text{GeTe}_2$  by a 30-min treatment (from 145 K to 90 K) clearly indicates that more than one layer of the sample degraded, which will be further discussed later.

For 2D  $\text{Fe}_3\text{GeTe}_2$  samples, the general trend is that the treatments cause the zero-field cooling induced RMCD signal at 80 K to decrease, as shown in Fig. 2c, d. Theoretically, the decreased RMCD may arise from two reasons. First, the optical reflectance of  $\text{Fe}_3\text{GeTe}_2$  may be altered by treatments. Specifically, the RMCD would change if the optical reflectance of left and right circularly polarized lights are affected differently by treatments. In this scenario, the evolution of RMCD reflects the evolution of samples’ optical properties, not necessarily the samples’ magnetic

properties. Second, the RMCD will certainly change if the magnetization of  $\text{Fe}_3\text{GeTe}_2$  is affected by treatments. The first scenario of the optical property change cannot account for the monotonic decrease of the RMCD signal for the progressively treated 4 L  $\text{Fe}_3\text{GeTe}_2$  as shown in Fig. 2c, for the saturated RMCD signals of the same set of treated 4 L  $\text{Fe}_3\text{GeTe}_2$  (see Fig. 4b) do not exhibit a monotonic decrease. Therefore, the treatment-induced decrease in RMCD in Fig. 2c reflects the decreased magnetization of the treated 4 L  $\text{Fe}_3\text{GeTe}_2$ .

### Ambient effect on the magnetic domains in few-layer $\text{Fe}_3\text{GeTe}_2$

We further analyzed the ambient effects on magnetic domain behaviors by normalizing the zero-field cooling induced RMCD ( $M_{ZFC}$ ) to the saturated RMCD ( $M_S$ ) at 80 K (see Fig. 2e). These fractional ratios indicate the domain formations in the zero-field cooling process (Note that the measurement of the bulk sample is conducted at 120 K as the coercivity field of the bulk  $\text{Fe}_3\text{GeTe}_2$  at 80 K becomes larger than our affordable magnetic field). First, for untreated bulk  $\text{Fe}_3\text{GeTe}_2$ ,  $M_{ZFC}$  is 90% of  $M_S$ , indicating the formation of an almost single domain within the laser spot size. However, for untreated thinner samples, the ratio drops noticeably to ~60% for both the 8 L and 4 L ones, and further drops to ~30% for the 3 L one, indicating the increasing tendency to form multiple domains under the laser spot for thinner samples (at 80 K).

It is also clear that the ambient effects promote the formation of multiple domains more for thinner samples than for thicker samples. As shown in Fig. 2e, the 30-min treatment causes negligible effects on the  $M_{ZFC}/M_S$  ratio for the bulk, but reduces the ratio for the 8 L sample by 12% (from 60% to 48%) and that for the 4 L sample by 50% (from 62% to 12%). For the 3 L sample, a quick 5-min treatment reduces the  $M_{ZFC}/M_S$  ratio by 17% (from 31% to 14%). This suggests the treatments cause more nucleation sites on the surface of thin  $\text{Fe}_3\text{GeTe}_2$  for the formation of multiple magnetic domains (as illustrated in the inset of Fig. 2e). The less ambient effects on the domain formation in thicker samples are likely caused by the less reaction between the air and thicker samples. It is also possible that the exchange coupling between different “puddles” of the reacted surface of thick samples can be maintained via the layers underneath, leading to the larger-size domain in thicker samples than in thinner samples.

To directly visualize the magnetic domains and the ambient effect on the domain formation, we scanned the RMCD images of another 4 L  $\text{Fe}_3\text{GeTe}_2$  sample (different from the 4 L sample in Figs. 1, 2, and 4) at 130 K after the zero-field cooling process. The

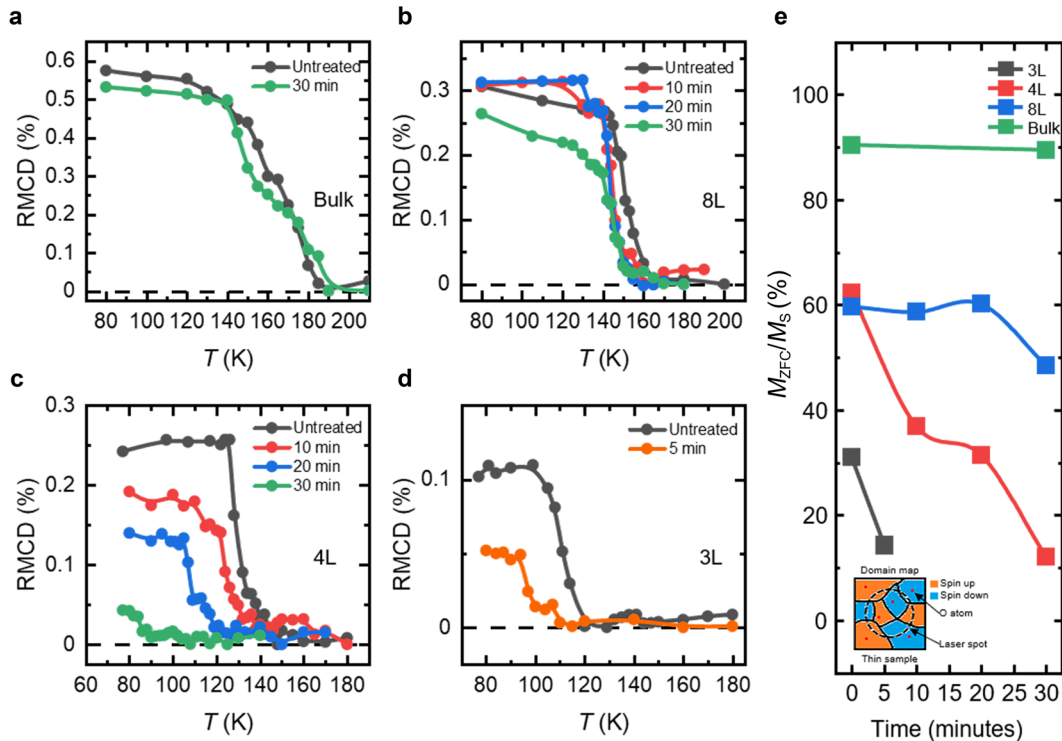


**Fig. 2** Temperature-dependent RMCD of  $\text{Fe}_3\text{GeTe}_2$  of different thicknesses with progressive treatments and the treatment- and thickness-dependent magnetic domain behaviors. **a–d** Temperature-dependent RMCD of bulk, 8 L, 4 L, and 3 L  $\text{Fe}_3\text{GeTe}_2$  with progressive treatments, respectively. The temperature-dependent magnetizations are done in the zero-field cooling process. **e** Ratio of the zero-field cooling induced magnetization and the saturated magnetization at 80 K as a dependence of the treatment duration for 8 L, 4 L, and 3 L  $\text{Fe}_3\text{GeTe}_2$  samples, respectively. For bulk samples, the data in (**e**) is taken at 120 K, as the coercivity field of bulk  $\text{Fe}_3\text{GeTe}_2$  at 80 K becomes larger than our affordable magnetic field. The inset of (**e**) is an illustration of multiple magnetic domains in 2D  $\text{Fe}_3\text{GeTe}_2$ , promoted by the oxygen adsorbates.

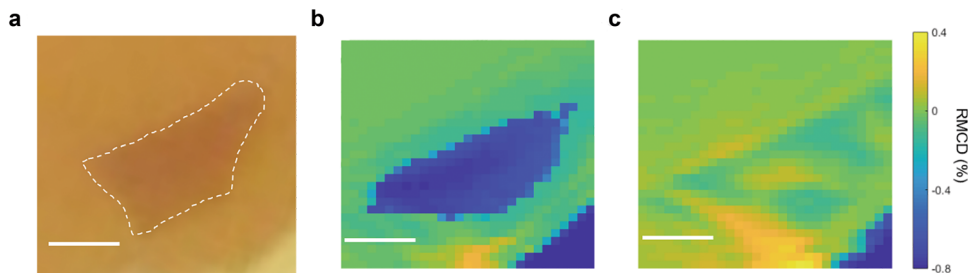


**Fig. 3** Optical image and magnetic domain patterns of a 4 L  $\text{Fe}_3\text{GeTe}_2$ . **a** 4 L  $\text{Fe}_3\text{GeTe}_2$  flake whose contour is circled out in the white dashed line. **b, c** Scanned RMCD images of the corresponding 4 L flake before and after a 10-min treatment, respectively. The data is taken at 130 K upon a zero-field cooling. Scale bars in (**a**)–(**c**), 3  $\mu\text{m}$ .

appearance of multiple adjacent yellow and light blue regions of irregular shapes after a 10-min treatment (as shown in Fig. 3c) is in stark contrast with a nearly uniform blue area before the treatment (as shown in Fig. 3b), clearly showing the emergence of multiple magnetic domains in the treated 4 L  $\text{Fe}_3\text{GeTe}_2$  (the optical image shown in Fig. 3a). This result serves as direct evidence that the ambient treatment promotes the formation of multiple magnetic domains.

The thickness-dependent ambient effects are also evident in the evolution of the coercivity fields. Consistent with the  $T_C$  behaviors, the coercivity field of the 8 L sample decreases slightly in the initial exposure to the air (i.e., the first 10-minute treatment) and tends to stabilize in additional 10-min and 20-min treatments, as shown in Fig. 4a, d. However, for the 4 L sample, the coercivity field drops quickly and monotonically with the progressive treatments, and becomes vanishingly small upon a 30-min treatment, as shown in Fig. 4b, e. More strikingly, for the 3 L sample, a 5-min treatment

already causes a substantial reduction of the coercivity field (see Fig. 4f). For each sample, treatments do not cause obvious changes in the linear slopes of the temperature-dependent coercivity fields in the temperature range well below  $T_C$ , which indicates the probed magnetism arises from the undegraded  $\text{Fe}_3\text{GeTe}_2$  sheets. This provides evidence that the treatments do not cause the degradation of all  $\text{Fe}_3\text{GeTe}_2$  layers as a whole, but primarily of the surface layers.

As pointed out above, the  $T_C$  drop of the 4 L  $\text{Fe}_3\text{GeTe}_2$  by the 30-min treatment (from 145 K to 90 K) clearly indicates that more than one layer of the sample degraded, which suggests the degradation can occur from both top and bottom surfaces. Due to the well-known  $\text{SiO}_2$  surface roughness and the weak coupling between exfoliated 2D materials and  $\text{SiO}_2$ , the space between 2D flakes and  $\text{SiO}_2$  allows the air to diffuse into the rough interface and trigger the degradation of 2D flakes from underneath. One prior study showed that the substrate-induced roughness<sup>21</sup>

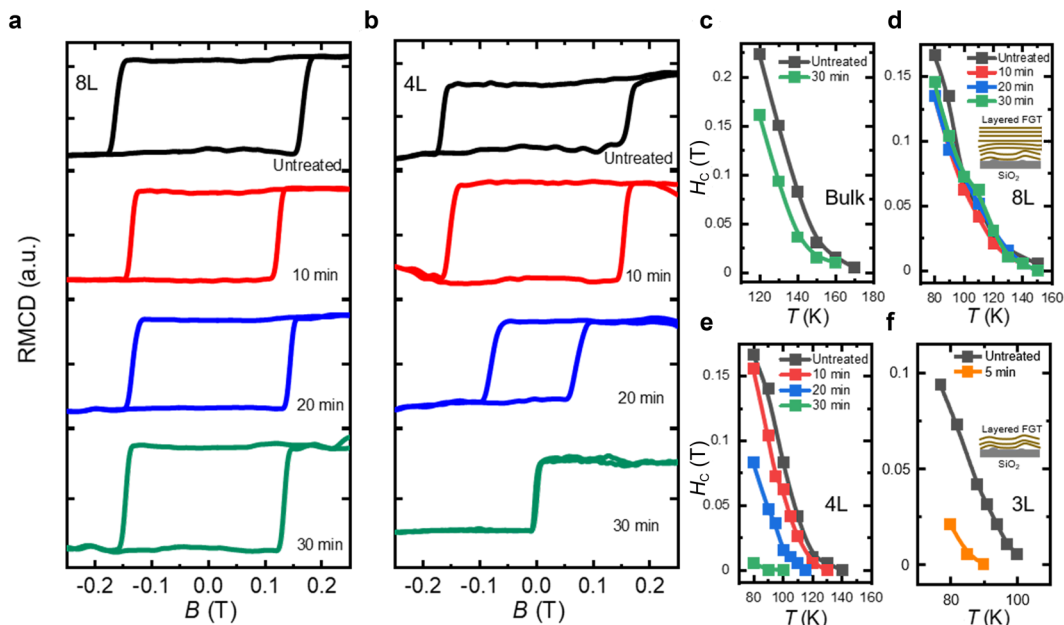


**Fig. 4** Magnetic hysteresis loops and temperature-dependent coercivity fields of  $\text{Fe}_3\text{GeTe}_2$  samples of different thicknesses. **a, b** Magnetic hysteresis loops at 80 K for the 8 L and 4 L  $\text{Fe}_3\text{GeTe}_2$  samples with progressive treatments. **c–f** Temperature-dependent coercivity fields of the bulk, 8 L, 4 L, and 3 L  $\text{Fe}_3\text{GeTe}_2$  samples with progressive treatments. The insets of **(d), (f)** show the top surfaces of thick and thin  $\text{Fe}_3\text{GeTe}_2$  samples on  $\text{SiO}_2$  are relatively flat and rough, respectively.

activates the single-layer graphene and promotes its etching much faster than bulk graphite<sup>22</sup>, of which the topmost graphene sheet has decoupled from the rough  $\text{SiO}_2$  substrate and remained chemically inert (as illustrated in the insets of Fig. 4d, f).

#### Modeling and calculation via density functional theory (DFT)

Our DFT<sup>23,24</sup> calculation includes the biaxial strain to model the local structure of a rough 2D  $\text{Fe}_3\text{GeTe}_2$ . Under biaxial strain ranging from  $-2\%$  to  $2\%$ , we calculated the dissociative adsorption energy of an  $\text{O}_2$  molecule on  $\text{Fe}_3\text{GeTe}_2$ ,  $E_{\text{ads},\text{O}_2}$ , which is defined as  $E_{\text{ads},\text{O}_2} = 2E_{\text{Fe}_3\text{GeTe}_2+\text{O}} - (2E_{\text{Fe}_3\text{GeTe}_2} + E_{\text{O}_2})$ , where  $E_{\text{Fe}_3\text{GeTe}_2+\text{O}}$ ,  $E_{\text{Fe}_3\text{GeTe}_2}$ , and  $E_{\text{O}_2}$  are the total energies of an O adsorbate on monolayer  $\text{Fe}_3\text{GeTe}_2$ , monolayer  $\text{Fe}_3\text{GeTe}_2$ , and  $\text{O}_2$  molecule, respectively. There are three different oxygen adsorption sites (i.e., Fe-top, Ge-top, and Te-top sites) on the  $\text{Fe}_3\text{GeTe}_2$  (see Fig. 5a). As shown in Fig. 5b, the dissociative adsorption of an  $\text{O}_2$  molecule on the Fe-top site (blue curve) is most energetically favorable. Given that the  $\text{SiO}_2$  roughness primarily causes the stretching strain in 2D flakes rather than compressive strain (note: the compressive strain would cause buckling or folding of 2D flakes), the stretching strain is practically more relevant. The blue curve in Fig. 5b shows that the stretching strain promotes the dissociative adsorption of  $\text{O}_2$  into oxygen adsorbates on Fe-top sites of  $\text{Fe}_3\text{GeTe}_2$ .

In addition to the strain effect, chalcogen vacancies ( $V_{\text{Te}}$  here) are commonly formed in exfoliated 2D flakes and make the defective surface more reactive than the pristine surface. The large adsorption energy variance of oxygen on different sites (see Fig. 5b) reveals a sizable oxygen diffusion barrier on  $\text{Fe}_3\text{GeTe}_2$ , which makes the oxygen adsorbates not mobile. Therefore, the buried layers in thick  $\text{Fe}_3\text{GeTe}_2$  will not be easily accessible by oxygen and will remain intact. We further calculated the kinetic barriers of the  $\text{O}_2$  adsorption and decomposition on  $\text{Fe}_3\text{GeTe}_2$  by the climbing image nudged elastic band (CI-NEB) method<sup>25</sup>. Fig. 5c shows the presence of substantial kinetic barriers during  $\text{O}_2$  adsorption and dissociation processes on the pristine  $\text{Fe}_3\text{GeTe}_2$  (the black and blue curves). In contrast, the oxygen reaction with the defective  $\text{Fe}_3\text{GeTe}_2$  (the red curve in Fig. 5c) exhibits low

kinetic barriers of 0.4 eV and 0.2 eV, indicating the easy reaction between the defective  $\text{Fe}_3\text{GeTe}_2$  and  $\text{O}_2$ . Once the  $\text{O}_2$  molecules decompose and fill the  $V_{\text{Te}}$ , the final states have even lower energy than the pristine  $\text{Fe}_3\text{GeTe}_2$ , preventing further degradations.

#### DISCUSSION

In summary, our systematic study of the metallic vdW magnet  $\text{Fe}_3\text{GeTe}_2$  shows the prominent thickness-dependent ambient effects. The Curie temperatures of the 3 L and 4 L  $\text{Fe}_3\text{GeTe}_2$  continuously drop as the samples are exposed to the air, but the Curie temperature of the 8 L  $\text{Fe}_3\text{GeTe}_2$  only drops by 10 K in the initial exposure and tends to stabilize afterward. The ambient treatments are found to effectively promote the formation of multiple magnetic domains in 2D  $\text{Fe}_3\text{GeTe}_2$ , but not in bulk  $\text{Fe}_3\text{GeTe}_2$ . Our DFT calculations suggest the roles of the stretched lattice (due to the rough  $\text{SiO}_2$  surface) and atomic vacancies (commonly existing in exfoliated 2D materials) in boosting the oxygen adsorption on and reaction with 2D  $\text{Fe}_3\text{GeTe}_2$ . The oxidized surface of bulk  $\text{Fe}_3\text{GeTe}_2$  prevents the layers underneath from further degradation. The understanding of the air-catalyzed evolution of Curie temperatures and magnetic domain behaviors of 2D magnets provides the scientific community with fundamental insights on chemically decorating and manipulating 2D magnets.

#### METHODS

##### Sample preparation

The bulk  $\text{Fe}_3\text{GeTe}_2$  single crystals were synthesized by the chemical vapor transport method, and few-layer samples were mechanically exfoliated and deposited on 260-nm-thick- $\text{SiO}_2/\text{Si}$  chips. The 2D samples were systematically heated on a hot plate (50 °C) in laboratory ambient conditions.

##### RMCD characterization

The RMCD characterization of magnetization was conducted by focusing a stabilized HeNe laser (633 nm) on the samples loaded in the Linkam



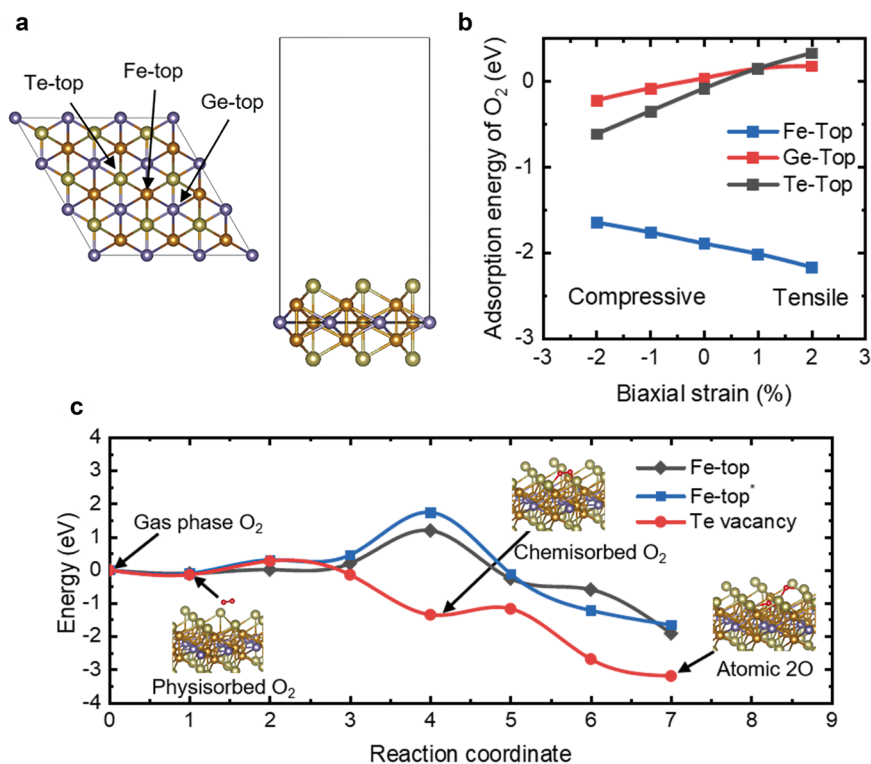


**Fig. 5 Modeling and calculation of the strain and Te vacancy effects on oxygen adsorption on monolayer Fe<sub>3</sub>GeTe<sub>2</sub>.** Supplementary Fig. 2 shows the detailed geometry of each structure after relaxation. **a** Top (left panel) and side (right panel) views of the atomistic configuration of the supercell of monolayer Fe<sub>3</sub>GeTe<sub>2</sub>. **b** Site-dependent dissociative adsorption energy of O<sub>2</sub> on Fe<sub>3</sub>GeTe<sub>2</sub> as a function of the biaxial strain. **c** Oxygen dissociative adsorption kinetics on the pristine Fe<sub>3</sub>GeTe<sub>2</sub> (black and blue curves) and a defective Fe<sub>3</sub>GeTe<sub>2</sub> with Te vacancy (i.e., V<sub>Te</sub>, red curve). Insets display the relaxed configurations of the physisorbed O<sub>2</sub>, chemisorbed O<sub>2</sub>, and dissociated 2O atoms on the defective Fe<sub>3</sub>GeTe<sub>2</sub> with V<sub>Te</sub>, respectively. Two different configurations of atomic 2O near Fe-top sites (Fe-top and Fe-top\* in the legend of (c)) are chosen as the possible final states on the pristine Fe<sub>3</sub>GeTe<sub>2</sub>, where Fe-top\* indicates the configuration of higher energy.

cooling/heating stage (results in Figs. 1, 2, and 4) and the Montana cryostat (scanning results in Fig. 3). With a homemade protruded sample stage, the samples are placed at the center of an external electromagnet coil. An objective of numerical aperture 0.5 was used to focus the beam down to a sub-micrometer spot size on the samples. The reflected light was collected by the same objective and detected by a photodiode. The helicity of the indicant light was modulated between left and right by a photoelastic modulator at 50 kHz. The MCD was determined by the ratio of an AC signal at 50 kHz (measured by a lock-in amplifier) and a low-frequency AC signal at 237 Hz (measured by another lock-in amplifier) of the reflected light intensity.

### DFT calculation method

Our first-principles calculations are based on DFT<sup>23,24</sup> using Vienna ab initio simulation package (VASP)<sup>26,27</sup>. For the exchange-correlation energy, we adopt the Perdew–Burke–Ernzerhof (PBE) functional<sup>28</sup> in the generalized gradient approximation (GGA). Pseudopotentials are given by the projector-augmented wave (PAW) method<sup>29,30</sup>. The energy cutoff for the plane-wave basis set is set to 300 eV, and spin-polarized calculations are performed. A 3 × 3 × 1 supercell of the monolayer Fe<sub>3</sub>GeTe<sub>2</sub> is prepared, including a 15-Å-thick vacuum region. A Monkhorst–Pack *k*-point grid of 4 × 4 × 1 is adopted for the Brillouin zone sampling. The atomic coordinates of an O atom or an O<sub>2</sub> molecule adsorbed on Fe<sub>3</sub>GeTe<sub>2</sub> are relaxed within a fixed cell shape and volume until the maximum atomic force is smaller than 0.02 eV Å<sup>-1</sup>.

### DATA AVAILABILITY

The data that support the findings of this study are available from the corresponding author upon reasonable request.

Received: 15 March 2021; Accepted: 7 June 2021;

Published online: 28 June 2021

### REFERENCES

- Gong, C. et al. Discovery of intrinsic ferromagnetism in two-dimensional van der Waals crystals. *Nature* **546**, 265–269 (2017).
- Huang, B. et al. Layer-dependent ferromagnetism in a van der Waals crystal down to the monolayer limit. *Nature* **546**, 270–273 (2017).
- Gong, C. & Zhang, X. Two-dimensional magnetic crystals and emergent heterostructure devices. *Science* **363**, eaav4450 (2019).
- Burch, K. S., Mandrus, D. & Park, J.-G. Magnetism in two-dimensional van der Waals materials. *Nature* **563**, 47–52 (2018).
- Gibertini, M., Koperski, M., Morpurgo, A. & Novoselov, K. Magnetic 2D materials and heterostructures. *Nat. Nanotechnol.* **14**, 408–419 (2019).
- Schedin, F. et al. Detection of individual gas molecules adsorbed on graphene. *Nat. Mater.* **6**, 652–655 (2007).
- Amani, M. et al. Near-unity photoluminescence quantum yield in MoS<sub>2</sub>. *Science* **350**, 1065–1068 (2015).
- Li, L. et al. Black phosphorus field-effect transistors. *Nat. Nanotechnol.* **9**, 372 (2014).
- Liu, H. et al. Phosphorene: an unexplored 2D semiconductor with a high hole mobility. *ACS Nano* **8**, 4033–4041 (2014).
- Shcherbakov, D. et al. Raman spectroscopy, photocatalytic degradation, and stabilization of atomically thin chromium tri-iodide. *Nano Lett.* **18**, 4214–4219 (2018).
- Nair, R. et al. Dual origin of defect magnetism in graphene and its reversible switching by molecular doping. *Nat. Commun.* **4**, 1–6 (2013).
- May, A. F., Calder, S., Cantoni, C., Cao, H. & McGuire, M. A. Magnetic structure and phase stability of the van der Waals bonded ferromagnet Fe<sub>3-x</sub>GeTe<sub>2</sub>. *Phys. Rev. B* **93**, 014411 (2016).
- May, A. F. et al. Ferromagnetism near room temperature in the cleavable van der Waals crystal Fe<sub>3</sub>GeTe<sub>2</sub>. *ACS Nano* **13**, 4436–4442 (2019).

14. Seo, J. et al. Nearly room temperature ferromagnetism in a magnetic metal-rich van der Waals metal. *Sci. Adv.* **6**, eaay8912 (2020).
15. Tan, C. et al. Hard magnetic properties in nanoflake van der Waals  $\text{Fe}_3\text{GeTe}_2$ . *Nat. Commun.* **9**, 1–7 (2018).
16. Fei, Z. et al. Two-dimensional itinerant ferromagnetism in atomically thin  $\text{Fe}_3\text{GeTe}_2$ . *Nat. Mater.* **17**, 778–782 (2018).
17. Deng, Y. et al. Gate-tunable room-temperature ferromagnetism in two-dimensional  $\text{Fe}_3\text{GeTe}_2$ . *Nature* **563**, 94–99 (2018).
18. Zhuang, H. L., Kent, P. & Hennig, R. G. Strong anisotropy and magnetostriction in the two-dimensional Stoner ferromagnet  $\text{Fe}_3\text{GeTe}_2$ . *Phys. Rev. B* **93**, 134407 (2016).
19. Liu, S. et al. Wafer-scale two-dimensional ferromagnetic  $\text{Fe}_3\text{GeTe}_2$  thin films grown by molecular beam epitaxy. *npj 2D Mater. Appl.* **1**, 30 (2017).
20. Weber, D., Trout, A. H., McComb, D. W. & Goldberger, J. E. Decomposition-induced room-temperature magnetism of the Na-intercalated layered ferromagnet  $\text{Fe}_{3-x}\text{GeTe}_2$ . *Nano Lett.* **19**, 5031–5035 (2019).
21. Lui, C. H., Liu, L., Mak, K. F., Flynn, G. W. & Heinz, T. F. Ultraflat graphene. *Nature* **462**, 339–341 (2009).
22. Liu, L. et al. Graphene oxidation: thickness-dependent etching and strong chemical doping. *Nano Lett.* **8**, 1965–1970 (2008).
23. Hohenberg, P. & Kohn, W. Inhomogeneous electron gas. *Phys. Rev.* **136**, B864 (1964).
24. Kohn, W. & Sham, L. J. Self-consistent equations including exchange and correlation effects. *Phys. Rev.* **140**, A1133 (1965).
25. Henkelman, G., Uberuaga, B. P. & Jónsson, H. A climbing image nudged elastic band method for finding saddle points and minimum energy paths. *J. Chem. Phys.* **113**, 9901–9904 (2000).
26. Kresse, G. & Furthmüller, J. Efficiency of ab-initio total energy calculations for metals and semiconductors using a plane-wave basis set. *Comput. Mater. Sci.* **6**, 15–50 (1996).
27. Kresse, G. & Furthmüller, J. Efficient iterative schemes for ab initio total-energy calculations using a plane-wave basis set. *Phys. Rev. B* **54**, 11169–11186 (1996).
28. Perdew, J. P., Burke, K. & Ernzerhof, M. Generalized gradient approximation made simple. *Phys. Rev. Lett.* **77**, 3865–3868 (1996).
29. Blöchl, P. E. Projector augmented-wave method. *Phys. Rev. B* **50**, 17953–17979 (1994).
30. Kresse, G. & Joubert, D. From ultrasoft pseudopotentials to the projector augmented-wave method. *Phys. Rev. B* **59**, 1758–1775 (1999).

## ACKNOWLEDGEMENTS

This work was primarily supported by C.G.'s startup grant from the University of Maryland, College Park. C.G. acknowledges the support from Northrop Grumman Mission Systems' University Research Program. Y.L. and K.C. were supported by the National Research Foundation (NRF) of Korea by Creative Materials Discovery Program (2015M3D1A1068062) and Nano Materials Technology Development Program (2016M3A7B4909942). The DFT calculations are performed with super-computing resources at the Texas Advanced Computing Center (TACC). I.T. was funded by ONR MURI N00014172661. N.V. and J.Z. would like to acknowledge the support of the Australian Research Council (ARC) Discovery Project and the Australian

Research Council Center of Excellence in Future Low-Energy Electronics Technologies (Project No. CE170100039). The work at Rutgers University was supported by the NSF under Grant No. DMR-1629059.

## AUTHOR CONTRIBUTIONS

C.G. conceived the project and designed experiments. T.X. conducted 2D sample exfoliation and MCD measurements under C.G.'s supervision. Y.L. carried out DFT calculations under K.C.'s supervision. J.Z. carried out AFM measurements under N.V. and I.T.'s supervision. A.S.A. synthesized bulk  $\text{Fe}_3\text{GeTe}_2$  crystals under S.-W.C.'s supervision. Y.G. and J.C. participated in the result discussion. C.G. and Z.T. wrote the manuscript with experimental figures provided by T.X. and DFT calculation figures and paragraphs provided by Y.L. and K.C. All authors approved the manuscript submission.

## COMPETING INTERESTS

The authors declare no competing interests.

## ADDITIONAL INFORMATION

**Supplementary information** The online version contains supplementary material available at <https://doi.org/10.1038/s41699-021-00242-z>.

**Correspondence** and requests for materials should be addressed to C.G.

**Reprints and permission information** is available at <http://www.nature.com/reprints>

**Publisher's note** Springer Nature remains neutral with regard to jurisdictional claims in published maps and institutional affiliations.



**Open Access** This article is licensed under a Creative Commons Attribution 4.0 International License, which permits use, sharing, adaptation, distribution and reproduction in any medium or format, as long as you give appropriate credit to the original author(s) and the source, provide a link to the Creative Commons license, and indicate if changes were made. The images or other third party material in this article are included in the article's Creative Commons license, unless indicated otherwise in a credit line to the material. If material is not included in the article's Creative Commons license and your intended use is not permitted by statutory regulation or exceeds the permitted use, you will need to obtain permission directly from the copyright holder. To view a copy of this license, visit <http://creativecommons.org/licenses/by/4.0/>.

© The Author(s) 2021